Journal of
Synchrotron
Radiation

ISSN 1600-5775

Received 2 December 2013
Accepted 29 March 2014

Development of a microsecond X-ray protein footprinting facility at the Advanced Light Source

Sayan Gupta,[a] Richard Celestre,[b] Christopher J. Petzold,[c] Mark R. Chance[d] and Corie Ralston[a]*

[a]Berkeley Center for Structural Biology, Physical Biosciences Division, Lawrence Berkeley National Laboratory, 1 Cyclotron Road, Berkeley, CA 94720, USA, [b]Experimental Systems, Advanced Light Source Division, Lawrence Berkeley National Laboratory, 1 Cyclotron Road, Berkeley, CA 94720, USA, [c]Joint BioEnergy Institute, Physical Biosciences Division, Lawrence Berkeley National Laboratory, 1 Cyclotron Road, Berkeley, CA 94720, USA, and [d]Center for Synchrotron Biosciences, Center for Proteomics and Bioinformatics, School of Medicine, Case Western Reserve University, Cleveland, OH 44106, USA. *E-mail: cyralston@lbl.gov

X-ray footprinting (XF) is an important structural biology tool used to determine macromolecular conformations and dynamics of both nucleic acids and proteins in solution on a wide range of timescales. With the impending shut-down of the National Synchrotron Light Source, it is ever more important that this tool continues to be developed at other synchrotron facilities to accommodate XF users. Toward this end, a collaborative XF program has been initiated at the Advanced Light Source using the white-light bending-magnet beamlines 5.3.1 and 3.2.1. Accessibility of the microsecond time regime for protein footprinting is demonstrated at beamline 5.3.1 using the high flux density provided by a focusing mirror in combination with a micro-capillary flow cell. It is further reported that, by saturating samples with nitrous oxide, the radiolytic labeling efficiency is increased and the imprints of bound *versus* bulk water can be distinguished. These results both demonstrate the suitability of the Advanced Light Source as a second home for the XF experiment, and pave the way for obtaining high-quality structural data on complex protein samples and dynamics information on the microsecond timescale.

Keywords: microsecond irradiation; radiolytic labeling; mass spectrometry; protein structure.

1. Introduction

For the past decade, X-ray footprinting (XF) has been used to study the structure and dynamics of a variety of macromolecules from small globular proteins to large macromolecular assemblies (Adilakshmi *et al.*, 2006, 2009; Angel *et al.*, 2009; Chaudhuri *et al.*, 2011; Dhavan *et al.*, 2002; Guan *et al.*, 2005; Kamal *et al.*, 2007; Kiselar *et al.*, 2003*b*; Sclavi *et al.*, 1998*a*; Adilakshmi *et al.*, 2008; Padayatti *et al.*, 2013; Gupta *et al.*, 2010; Oztug Durer *et al.*, 2011; Bohon *et al.*, 2008). The XF technique, like other hydroxyl radical (•OH) based footprinting approaches, utilizes •OH as a probe to cleave solvent-accessible nucleic acid backbones or covalently label amino acid side chains; the former are analyzed by sequencing methods and the latter are analyzed by mass-spectrometry-based bottom-up proteomics (Xu & Chance, 2007; Kiselar & Chance, 2010; Gupta *et al.*, 2007*a*). Other methods, such as laser photochemical and electrospray ionization, also generate •OH in protein solutions (Aye *et al.*, 2005; Hambly & Gross, 2005). In the laser photochemical method, a sufficient amount of •OH for covalent labeling is produced on the microsecond timescale, and one drawback of this method is that it requires a millimolar concentration of hydrogen peroxide, which can unfold proteins and/or perturb complex protein assemblies with metal active centers (Watson *et al.*, 2009; Ling *et al.*, 2012; Shacter, 2000). The electrospray ionization method was first proposed and demonstrated over a decade ago and has been used to study structure and dynamics of a number of biological systems (Maleknia *et al.*, 1999; Maleknia & Downard, 2001). The method uses a very high voltage in the presence of O_2 to produce •OH radicals in protein solutions in the presence of volatile buffer components (Downard *et al.*, 2012; Konermann *et al.*, 2013; Laganowsky *et al.*, 2013; Maleknia *et al.*, 1999; Maleknia & Downard, 2001, 2012; Wong *et al.*, 2005). All the radical-generating techniques have unique advantages and disadvantages, and therefore should be applied variously depending on the system under study. In XF, •OH is generated *in situ* by ionizing irradiation, and can be used with aqueous buffered solutions near physiological conditions or inside living cells, and is therefore highly suitable for studying

membrane proteins and complex biomolecular systems, which are the major scientific drivers for the development of the XF method in coming years (Adilakshmi *et al.*, 2008; Angel *et al.*, 2009; Bohon *et al.*, 2008; Gupta *et al.*, 2010, 2014; Orban *et al.*, 2012; Padayatti *et al.*, 2013; Clatterbuck Soper *et al.*, 2013). In the XF method the extent of covalent labeling is increased with $^{\bullet}$OH concentration, which is related to X-ray irradiation time or dose. XF provides a straightforward way to vary the $^{\bullet}$OH dose from 5- to 20-fold by varying the flow rate of the sample across the fixed size and flux density of an X-ray beam. The global fitting of the corresponding dose-response plot is used to quantify hydroxyl radical reactivity of specific side chains, and the comparison of reactivity for various functional states provides information on the degree of solvent accessibility changes. This simple approach is highly advantageous in terms of handling multiple dose-dependent data and statistical data analysis for accurate comparisons between multiple states of complex biological samples.

Complex protein samples often require the presence of millimolar concentrations of cofactors (*e.g.* ATP), reducing agents (DTT) or other additives (*e.g.* glycerol, EDTA) for their optimum activity and stabilization (Bohon *et al.*, 2008; Oztug Durer *et al.*, 2011). Membrane protein samples require detergents or phospholipids for solubilization and reconstitution (Angel *et al.*, 2009; Gupta *et al.*, 2010). *In vivo* studies must be performed in growth medium or cell suspension buffer to maintain the optimum activity of the cells (Adilakshmi *et al.*, 2006, 2009; Clatterbuck Soper *et al.*, 2013), and these reagents act as extrinsic hydroxyl radical scavengers and reduce the effective hydroxyl radical dose possible (Gupta *et al.*, 2007*a*, 2010; Bohon *et al.*, 2008). Moreover, large macromolecular assemblies can themselves act as intrinsic scavengers of hydroxyl radicals. Therefore, it is often necessary to increase the irradiation time to generate a sufficient concentration of hydroxyl radicals to overcome the scavenging processes (Gupta *et al.*, 2007*a*, 2010; Bohon *et al.*, 2008). The low flux density of an unfocused X-ray beam from a bending-magnet source often necessitates exposure times as high as 200 ms (Kiselar *et al.*, 2003*a*; Gupta *et al.*, 2004, 2007*b*). However, long exposures result in secondary free-radical reactions, leading to protein damage and non-linearity of the dose-response plots. Limiting the exposure at the high end due to non-linearity and at the low end due to insufficient flux density leads to a very limited range of X-ray exposures, which in turn leads to uncertainty in data fitting. The advent of the use of a focused beam has revolutionized the XF approach at the NSLS white-light bending-magnet beamline X28C (Sullivan *et al.*, 2008), which now delivers significantly more usable flux density to the sample as compared with the unfocused beam, and allows researchers to carry out analysis of complex protein systems with irradiation times down to single-digit milliseconds (Angel *et al.*, 2009; Bohon *et al.*, 2008; Gupta *et al.*, 2010; Padayatti *et al.*, 2013; Orban *et al.*, 2012). However, a continuing major challenge in XF is the introduction of sufficient hydroxyl radical dose without prolonging exposure time. In order to address this challenge and extend the range of the XF technique below a millisecond, we have used a high-flux-density focused X-ray beam at the Advanced Light Source (ALS) in combination with a high-speed micro-capillary flow cell. The results obtained for a fluorescence standard, cytochrome-*c* (cyt *c*), and a megaDalton protein assembly illustrate the capabilities of beamline 5.3.1, which is able to generate sufficient protein labeling to conduct the XF experiment with microsecond exposures. In addition, we report that the increased labeling efficiency by purging protein sample solutions with N_2O gas under normal levels of oxygen concentration can be used to differentiate labeling events of bulk from bound water. These results show that advances in the X-ray radiolytic labeling technique can continue to be developed and XF users can be supported at the ALS beamlines while the NSLS II XF beamline is constructed.

2. Methods

2.1. Sample preparation

The 5 m*M* Alexa 488 fluorescence dye (Promega) and 10 µ*M* horse-heart cyt *c* (Sigma) were prepared in 10 m*M* phosphate buffer. The 1 µ*M* 1 MDa protein complex, a group II chaperonin from *Methanococcus maripaludis* (mmcpn) (Pereira *et al.*, 2010), was prepared in 10 m*M* sodium cacodylate containing 1 m*M* TCEP, 1 m*M* ATP, 5% glycerol and 120 m*M* NaCl. The N_2O/O_2 saturated cyt *c* solution was prepared by purging a N_2O/O_2 (4:1 *v*/*v*) gas mixture at a flow rate of 10 ml min^{-1} for 2 min ml^{-1} of sample solution.

2.2. Microfluidic capillary flow set-up

Polymicro fused silica capillaries of internal diameter (ID) 100 and 200 µm were used to flow the sample past the X-ray beam. Two capillaries, each 4.5 cm long, one for sample irradiation and the other for sample infusion from the syringe, were connected using Tygone® tubing (Fig. 1). The capillary for sample infusion was connected by zero dead volume fittings (Upchurch) to 1 ml and 2.5 ml gas-tight glass Luer-lock syringes. Tygone® tubing was used for ease of replacement of damaged sample irradiation capillaries, flexibility in a confined space, reduction of back pressure, and as a safety feature to prevent sample loss due to pump malfunction resulting from high back pressure during prolonged usage. A temperature-controlled sample mount for the microfludic flow tubes with outer diameter from 150 µm to 630 µm was constructed at the ALS. The sample mount consisted of four major components: (i) A base plate made from aluminium to connect the sample mount to a motorized stage for beam alignment. A ~75 µm depth groove served to guide the capillary into place during mounting. (ii) Flexible horizontal slits to hold the capillary horizontal to the beam and to measure vertical beam size. (iii) Flexible vertical slits to measure horizontal beam size. (iv) A water-cooled copper block to prevent heat-induced damage of samples during X-ray irradiation. A high-pressure syringe pump (Harvard, OEM 2200 module) with *FlowControl* software was used for accurate control of sample volume and speed. Samples were collected in microfuge tubes containing methionine amide as a radical scavenger. The irradiation

Table 1
Beam size, irradiation time and flow speed in the micro-capillary flow set-up.

Beam size†: ∼106 µm (H) × 164 µm (V) Tube ID: 100 µm Alexa rate‡: 13764 s^{-1}		Beam size: ∼210 µm (H) × 240 µm (V) Tube ID: 200 µm Alexa rate: 6000 s^{-1}		Beam size: ∼500 µm (H) × 600 µm (V) Tube ID: 535 µm Alexa rate: 6410 s^{-1}	
Flow speed (µl min^{-1})§	Irradiation time (µs)¶	Flow speed (µl min^{-1})	Irradiation time (µs)	Flow speed (µl min^{-1})	Irradiation time (µs)
3180	15	4940	100	4750	200
1590	30	1976	250	2375	400
795	60	988	500	1583	600
398	120	659	750	1188	800
199	240	494	1000	950	1000
99	480	198	2500	475	2000

† Beam size is measured from the derivative scan of photodiode intensity as shown in Fig. 2. ‡ Alexa rate is calculated from the representative dose-response plot shown in Fig. 4. § Maximum and minimum flow speed are dependent on the syringe size and syringe type, and the values are determined from the Harvard OEM 2200 module operation software *FlowControl* v1.0. ¶ Irradiation time is calculated using equation (1), using the parameters tube ID, flow speed and length as defined by the FWHM of the horizontal scan.

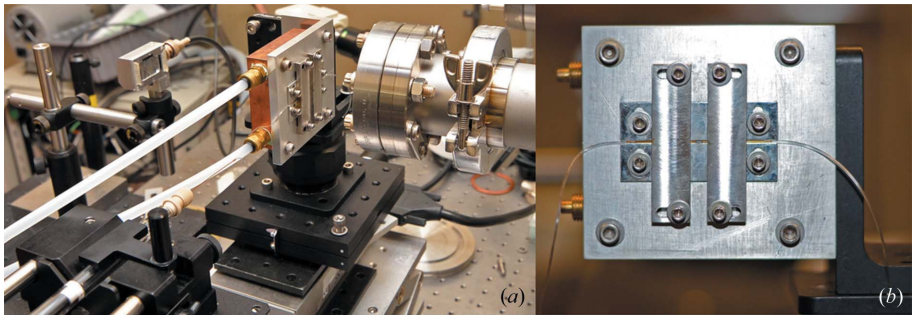

Figure 1
Microfluidic capillary flow set-up. (*a*) The portable set-up consists of a syringe pump (bottom left), water-cooled sample mount on a motorized stage (center) and photodiode (behind the sample mount). The sample mount is assembled close to the ultrahigh-vacuum beampipe which is capped with a beryllium window. (*b*) Front view of the temperature-controlled sample mount. The horizontal slits hold the capillary horizontal to the beam. The photodiode allows detection of attenuated beam through the aluminium sample mount, and the alignment of the capillary tube is carried out by horizontal and vertical slits.

time (t) was controlled by three key parameters: flow speed, exposure length (l, horizontal beam size) and tube ID, which are related by the following equation,

$$\text{Irradiation time } t\ [\mu s] = \frac{\pi \times (\text{ID}/2\ [\text{mm}])^2 \times l\ [\text{mm}] \times 60 \times 10^6}{\text{Flow speed}\ [\mu l\ min^{-1}]} \quad (1)$$

Table 1 provides a summary of the pump speed, size of the beam and corresponding irradiation times that were used for sample exposure using the microfluidic flow configuration, and the corresponding Alexa dose rates for a given beam size.

2.3. Sample irradiation

Radiolysis of samples was performed at ALS beamlines 5.3.1 and 3.2.1, and NSLS beamline X28C. ALS beamline 5.3.1, designed for qualifying X-ray optics (Yuan *et al.*, 2011), is located on a bending-magnet source and equipped with a platinum-coated toroidal focusing mirror suitable for focusing a white-light X-ray beam. The physical size of the mirror is 900 mm (length) × 65 mm (width) × 75 mm (depth), with a sagittal dip (edge to middle) of 7.8 mm, and motorized bend capability. Focusing of the X-ray beam is achieved by varying mirror tilt, bend and pitch angle. The broadband X-ray beam (1–13 keV) exits from the beryllium window of the beampipe under ultra-high vacuum, with a flux of ∼1 × 10^{16} photons s^{-1}. Various focused beam sizes were set to deliver homogeneous flux density to match micro-capillary sample tubes of 100–535 µm ID. The sample mount was attached to a motorized stage capable of horizontal and vertical scans, and a photodiode was used to detect the beam for beam alignment. Slits made of stainless steel at the sample mount were used for knife-edge scans to estimate the horizontal and vertical FWHM of the beam (Fig. 2). Irradiation times and corresponding beam sizes, flow speed and tubing sizes are shown in the Table 1. ALS beamline 3.2.1 is a white-light bending-magnet beamline with similar characteristics to 5.3.1 but with no focusing mirror; the beam size is fixed at ∼10 mm (V) × 100 mm (H). NSLS beamline X28C is located on a bending-magnet source,

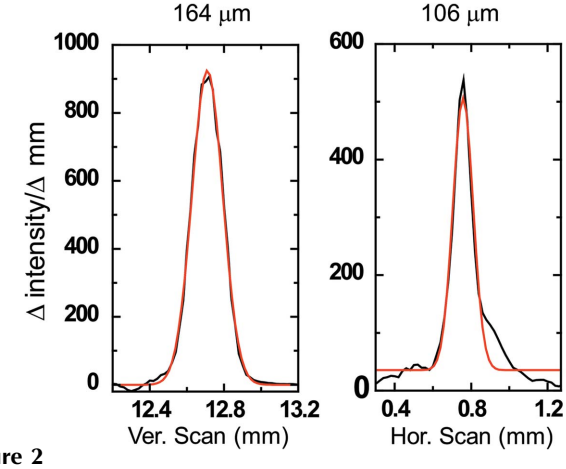

Figure 2
Beam profile and alignment. Horizontal and vertical profile of the focused beam at 5.3.1 is obtained by vertical and horizontal scans, respectively, using a single slit of the sample mount. The derivative of the photodiode signal is used to obtain the beam profile. The data (black line) are fitted to a Gaussian function (red line) to obtain the FWHM.

and is equipped with a palladium-coated toroidal focusing mirror (Sullivan *et al.*, 2008). The mirror was adjusted to create a beam of FWHM 0.5 mm × 0.5 mm to provide the highest flux density possible to use as a control X-ray source for our experiments at the ALS. Sample irradiation using the microfluidic set-up with 100 µm and 200 µm ID tubing in combination with a syringe pump was carried out in the same way as previously described (Bohon *et al.*, 2014).

2.4. Liquid chromatography: mass spectrometry data analysis

The samples exposed at ALS beamlines 3.2.1 and 5.3.1 were analyzed on an Agilent 6550 iFunnel Q-TOF mass spectrometer coupled to an Agilent 1290 LC system (Agilent Technologies, Santa Clara, CA, USA). Proteolytic digestion of cyt *c* and mmcpn was carried out using standard digestion methods with trypsin enzyme (Promega) overnight at 310 K at pH 8 in 50 m*M* ammonium bicarbonate buffer. Peptide samples were loaded onto a Sigma-Aldrich Ascentis Peptides ES-C18 column (2.1 mm × 100 mm, 2.7 µm particle size; Sigma-Aldrich, St Louis, MO, USA) *via* an Infinity Autosampler (Agilent) with buffer A (2% acetonitrile, 0.1% formic acid) flowing at 0.400 ml min^{-1}. Peptides were eluted into the mass spectrometer *via* a gradient with an initial condition of 5% buffer B (98% acetonitrile, 0.1% formic acid) increasing to 35% B over 6–20 min (for cyt *c* and mmcpn, respectively). Subsequently, B was increased to 90% over 1 min and held for 3 min at a flow rate of 0.6 ml min^{-1} followed by a ramp back down to 5% over 1 min where it was held for several minutes to re-equilibrate the column to the original condition. Peptides were introduced to the mass spectrometer from the LC using a Jet Stream source (Agilent) operating in positive-ion mode (3500 V). The data were acquired with MassHunter B.05.00 operating in Auto MS/MS mode whereby the three most intense ions (charge states 2–5) within a *m*/*z* 300–1400 mass range above a threshold of 1000 counts were selected for MS/MS analysis. MS/MS spectra were collected with the quadrupole set to 'Narrow' resolution and collision energy to optimize fragmentation. MS/MS spectra were scanned from *m*/*z* 100 to 1700 and collected until 40000 total counts were collected or for a maximum accumulation time of 333 ms. Parent ions were excluded for 0.1 min following MS/MS acquisition. MS/MS data of native and modified peptide fragments were interpreted by Mascot MS/MS Ions Search. The abundance of native and modified peptides at each irradiation time point were measured (peak area) from their respective extracted ion chromatogram using Agilent Mass Hunter version 2.0.

The cyt *c* samples exposed at NSLS beamline X28C and then digested by trypsin were analyzed by a Thermo-Fisher LCQ DecaXP Plus mass spectrometer interfaced with Waters Alliance 2695 HPLC according to standard LC-ESI-MS procedures. LC-MS/MS parameters were set for carrying out a full data-dependent scan. Peptide samples were loaded into a Vidac C-18 (1.5 mm × 150 mm, 5 µm particle size) *via* an inbuilt auto-sampler Waters Alliance 2695 HPLC with buffer A (5% acetonitrile, 0.1% TFA) flowing at 50 µl min^{-1}. Peptides were eluted into the mass spectrometer *via* a gradient starting from 100% buffer A to 2:8 (*v*/*v*) mixture of buffer A and buffer B (95% acetonitrile, 0.1% TFA) in 70 min. Subsequently, buffer B was increased to 100% for 20 min at the same flow rate followed by washing the column with 100% buffer B for 10 min. The column was re-equilibrated for 20 min with buffer A before loading the next sample. Peptides were introduced to the mass spectrometer using the ESI source operating in the positive-ion mode (5000 V). The data were acquired using *XCalibur* V2.1 operating in data-dependent MS/MS mode with separate scan events to carry out CID fragmentation of the four most intense ions (charge state 2–3) within the *m*/*z* range 300–2000. The mass spectrometer was programmed to collect data across narrow *m*/*z* ranges. In each *m*/*z* range the mass spectrometer was programmed to exclude previously analyzed ions starting with the most abundant ions to a set limit following a standard protocol. MS/MS spectra for the unmodified and modified peptides were manually interpreted with the aid of *ProteinProspector* (University of California, San Francisco, USA) and *Bioworks 3.3* software (Thermo Scientific). The abundance of native and modified peptides at any irradiation time point area were measured (peak area) from their respective selected ion chromatogram using *XCalibur* V2.1.

The fraction unmodified for each peptide was calculated as the ratio of the integrated peak area of the unmodified peptide to the sum of integrated peak areas from the modified and unmodified peptides. The dose-response curves (fraction unmodified *versus* X-ray exposure time) were fitted to single exponential functions in *Origin* version 7.5 (OriginLabs). The rate constant k (s^{-1}) was used to measure the reactivity of a chain towards hydroxyl radical induced modification.

3. Results and discussion

3.1. The necessity of a short irradiation time for radiolytic labeling of proteins in solution

The key reaction in the XF technique is the covalent labeling of protein side chains by •OH. The extent of reaction between protein and •OH or yield of covalent labeling depends on both the intrinsic reactivity and the solvent accessibility of the side-chain residues. Since footprinting compares two or more states of proteins, the changes in the amount of covalent labeling on the same residue from one state to another depends solely on the solvent accessibility difference between the two states. The solvent accessibility information is interpreted in the context of existing high-resolution structures and/or incorporated into molecular modeling strategies that provide information about conformational changes or substrate binding (Gupta *et al.*, 2010; Kamal *et al.*, 2007; Padayatti *et al.*, 2013; Kiselar *et al.*, 2007; Gerega & Downard, 2006; Kamal & Chance, 2008). Understanding the complex reaction steps in XF is important not only for improving the technique but also as it will lead to a broader application of the technique for a variety of sample conditions. A synchrotron X-ray source is capable of deli-

vering a wide range of photon energies, and while absorption of energy in dilute aqueous solution is energy-dependent, the footprinting experiment generally uses the entire range of photon energy delivered by a synchrotron beam in order to maximize absorbed dose. The timescale for the sequence of events in the radiolysis of pure water by ionizing radiation is well studied and shown in Fig. S1 of the supporting information (Liljenzin, 2002; Ralston *et al.*, 2000; Sclavi *et al.*, 1998*b*).[1] The ionization event that releases an electron occurs on the timescale of an electronic transition ($<10^{-16}$ s). The positive ion H_2O^+ reacts with H_2O within 10^{-15} s, forming an $^{\bullet}OH$ radical and H_3O^+. The excited water also dissociates directly to $^{\bullet}H$, H_2, $^{\bullet}O$ and $^{\bullet}OH$ (10^{-14}–10^{-13} s). The electron liberated with sufficient kinetic energy can further ionize water molecules and finally become solvated within 10^{-12} s. These radiolysis products, including the $^{\bullet}OH$ radicals, are clustered in spurs and inhomogeneously distributed in water before they start to diffuse out of the spur volume. Spur diffusion or expansion completes within the diffusion timescale (10^{-8}–10^{-7} s), and in this event several recombination reactions take place leading to the formation of secondary products (Fig. S2 of the supporting information). The major recombination reactions that are known to reduce footprinting yields are scavenging of $^{\bullet}OH$ [equations (2) and (3)], elimination of dissolved O_2 [equation (4)] required for covalent labeling of amino acid side chains in protein [equation (5) and Fig. S3], and the production of peroxides and superoxide [equations (2) and (4)] that damage or unfold protein molecules,

$$^{\bullet}OH + {}^{\bullet}OH = H_2O_2 \qquad (2)$$

$$\text{buffer/additives} + {}^{\bullet}OH = \text{modified or degraded buffer/additives} \qquad (3)$$

$$e^-_{aq} + O_2 = O_2^- \qquad (4)$$

$$-\text{NHCH(CH}R_2\text{)CO}- + {}^{\bullet}OH + O_2 = -\text{NHCH(COH}R_2\text{)CO}- + {}^{\bullet}OOH \qquad (5)$$

$^{\bullet}OH$ is a highly reactive species, reacting within one to five molecular diameters of the site of formation in the presence of reactants with bimolecular rate constants near diffusion-controlled processes (Pryor, 1986). The lifetime of the $^{\bullet}OH$ radical can be as short as a few microseconds in water, and is dependent on the concentration of reactive substrates in the vicinity of the radical (Hambly & Gross, 2005; Pryor, 1986; Watson *et al.*, 2009). One of the major losses of hydroxyl radical in bulk water occurs by diffusion-controlled bimolecular recombination between the hydroxyl radicals [equation (2), $\sim 5 \times 10^9\ M^{-1}\ s^{-1}$] (Buxton *et al.*, 1988; Janik *et al.*, 2007). In addition, protein solutions often require additives such as buffers, ATP or glycercol, which also act as reactive substrates [equation (3), rate constant $\simeq 10^9\ M^{-1}\ s^{-1}$] and contribute to a significant loss of $^{\bullet}OH$ (Buxton *et al.*, 1988). Certain amino acids, for example, Met, Cys, Trp, Tyr, Phe, His, Arg, Ile and Leu, when free in aqueous solution can react with $^{\bullet}OH$ extremely rapidly (rate constants 10^9–$10^{10}\ M^{-1}\ s^{-1}$); however, there is no report on their rate constants when within a folded protein [equation (5)] (Buxton *et al.*, 1988; Janik *et al.*, 2007). The rate can be altered depending on the accessibility of the side chain to $^{\bullet}OH$, and overall modification can be significantly diminished by the presence of the counter-productive processes of hydroxyl radical loss shown by equations (1) and (2). Therefore, maintaining a steady-state concentration of $^{\bullet}OH$ under any timescale requires a continuous radiation dose; generation of $^{\bullet}OH$ in XF is a flux-density-driven process. Fundamentally, with a given irradiation time, the higher the flux density then the greater the steady-state concentration of $^{\bullet}OH$, which results in greater yield of modification products.

Unlike in dilute solutions of amino acids or small polypeptides, which react with the available $^{\bullet}OH$ by a homogeneous kinetics process, $^{\bullet}OH$-induced modification in a large protein system follows a complex kinetic pathway (Fig. 3). A large protein creates distinct hydration environments that are different from that of the bulk water. The cavities, grooves and active sites in a protein contain hydrogen-bonding networks and ionic interlocks with amino acid side chains that can bind three times as many water molecules as the solvent-exposed surface (Kuhn *et al.*, 1992; Kuntz *et al.*, 1969). The XF technique has already been reported to selectively label amino acid residues adjacent to bound water (Angel *et al.*, 2009; Gupta *et al.*, 2012). Ion channels and receptors show modification in specific residues within the transmembrane domain where bound waters are located in contrast to having non-specific labeling of the solvent-exposed amino acid residues which are close to the bulk water molecules (Angel *et al.*, 2009; Gupta *et al.*, 2010). Thus, in many cases the $^{\bullet}OH$ reaction with amino acid side chains within complex proteins might not

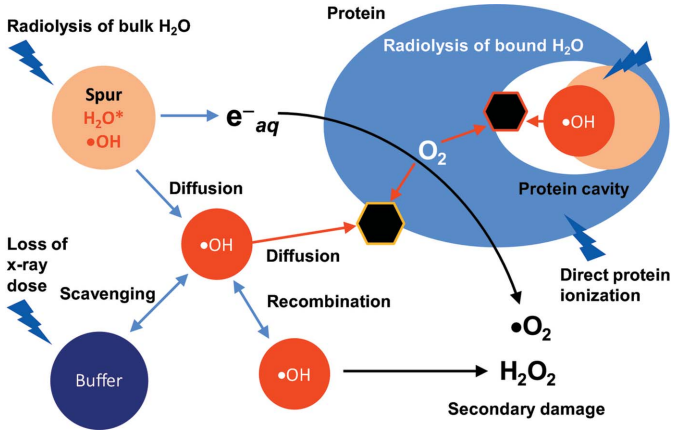

Figure 3
Schematics of major reactions for X-ray radiolysis in dilute protein samples. Radiolysis of bulk water starts with the ionization of water under 10^{-16} s (spur). The key product, $^{\bullet}OH$, diffuses (10^{-7} s) out in the bulk and undergoes reactions with the buffer and protein side chains. The former reaction, as well as various recombination reactions, scavenge $^{\bullet}OH$ and reduce the concentration of $^{\bullet}OH$ in the bulk. Sufficient X-ray dose is needed to maintain a steady-state concentration of $^{\bullet}OH$.

[1] Supporting information for this paper is available from the IUCr electronic archives (Reference: RV5012).

strictly follow homogeneous kinetic pathways; instead, the reaction can be strongly affected by the ionization of the local water in the vicinity of the reactive amino acid side chains (Pearson & Williams, 1987). At room temperature, delivering a high dose by prolonged irradiation time to overcome the loss of •OH does not necessarily result in more modification to those sites; instead, protein damage occurs by increase in heat load, depletion of O_2, generation of peroxides and degradation of buffer components, and this in turn results in deterioration of the mass spectrometry signal of both native and modified species. As indicated earlier, complex protein samples that require buffer conditions and additives that react with the •OH radical preferentially [equation (2)] reduce the effective dose to the protein. In those specific cases, prolonging the irradiation time is often necessary to overcome the loss of •OH; however, such high irradiation doses generate more solvated electrons, deplete O_2 and increase the peroxide levels, resulting in secondary damage to the sample. The secondary damage is time dependent and results in specific structural perturbation. In contrast, a high •OH concentration applied over a short timescale can preserve the structural integrity of complex protein assemblies as well as overcome the scavenging reactions in the buffer solution. Therefore, to extend the range of protein systems accessible to the XF experiment and simultaneously obtain high-quality data, it is necessary to use a combination of a focused synchrotron X-ray radiation beamline of high flux density, such as ALS beamline 5.3.1, with a high-speed capillary flow cell. In the following sections, results from beamline 5.3.1 are shown for a fluorophor, the small globular protein cyt *c* and a megaDalton protein complex.

3.2. Double-digit microsecond irradiation of Alexa 488 solution

A fluorescence dye was used as a dosimeter molecule to determine the effect of sample conditions on the generation of hydroxyl radicals by synchrotron radiolysis (Gupta *et al.*, 2007*a*; Xu & Chance, 2007). This method of estimation of dose is empirical, and has been used to optimize dosage conditions for complex protein samples for the past decade (Gupta *et al.*, 2010; Bohon *et al.*, 2008). In this assay the decrease in the fluorescence intensity of Alexa is monitored as a function of increasing irradiation time (Fig. 4). A considerable loss of fluorescence intensity was observed in the double-digit microsecond timescale when the solution was irradiated using a micro-capillary sample delivery of 100 µm ID flow path and high-flux-density beam of size 164 µm (V) × 106 µm (H). X-ray radiolysis of Alexa at ALS 5.3.1 showed up to a 30-fold increase in the rate of Alexa degradation in comparison with the typical NSLS X28C configuration with a KinTek® apparatus (400 s^{-1}, data not shown) and a greater than six-fold increase relative to that of the point focus beam (2000 s^{-1}, data not shown) of NSLS X28C with a similar micro-capillary set-up. The rate increase and gain in the shortest irradiation time (down to 15 µs) has been achieved by our collective approach of using high-speed sample delivery, narrow sample

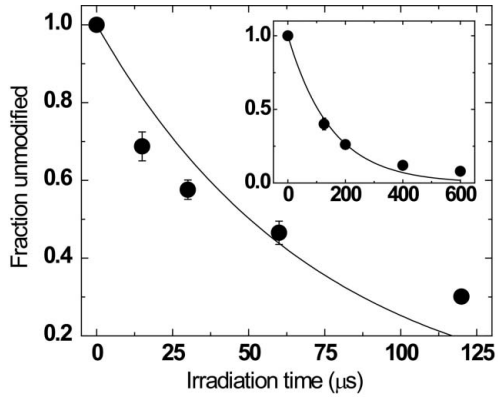

Figure 4
Microsecond irradiation of Alexa 488 solution. Dose response plot of 10 m*M* Alexa in 10 m*M* phosphate buffer, pH 7, using the 106 µm × 164 µm focused beam at ALS beamline 5.3.1. A 200 µL volume of Alexa solution was passed through the 100 µm ID capillary tube on the sample mount at different speeds (Table 1) to obtain irradiation times in the range 15–120 µs. Fluorescence analysis was carried out as previously described (Gupta *et al.*, 2007*a*). The solid line represents a single exponential fit with a rate constant k = 13764 s^{-1}, with individual points representing the mean of three independent measurements with standard error. The inset shows the dose-response plot of the same sample using a larger beam to irradiate samples homogeneously inside a 535 µm ID capillary tube, with an exponential fit rate constant of k = 6410 s^{-1}.

ID capillaries, and a high-flux-density focused beam. The major challenge with the current 100 µm ID set-up was difficulty in positioning the micro-capillary within the micrometer-size beam hot-spot, and breaking of the capillary tube due to the radiation-induced damage. Temperature measurements showed that the point focus beam at NSLS-X28C can increase the sample temperature at a rate 0.13 K ms^{-1} (Sullivan *et al.*, 2008). Therefore it can be estimated that the six-fold increase in the flux density at ALS increases the sample temperature by approximately <1 K ms^{-1} of irradiation. Breakage of the 100 µm ID capillary tube was caused by the total heat deposition under repeated usage; while the sample flowed past the beam on the order of microseconds to milliseconds, the tubing itself remained in the beam on the order of seconds to minutes during normal experimental conditions. These limitations can be overcome in the near future by microfabrication techniques and pre-shutter installation. Our results show the feasibility of extending the dose range to even faster irradiation times using an even more tightly focused beam and a nanoliter sample-handling system. The results in the following sections were carried out with a slightly defocused beam at 5.3.1 to ensure proper alignment and efficient heat exchange.

3.3. Labeling efficiency of cyt *c* at the ALS

To verify the quality and reproducibility of radiolytic labeling in protein samples at the ALS, beamline 5.3.1 was defocused to make the flux density identical to that of the point focus beam of X28C at NSLS. The comparison of the deliverable dose at the point focus beam of size 0.5 mm × 0.5 mm at beamline X28C of NSLS and the focused beam of

size 2 mm × 1 mm at ALS beamline 5.3.1 using 100 µm ID microfluidic sample cells was carried out by Alexa assay. The assay showed similar rate constants of ∼2000 s^{-1} in both beamlines and confirmed the identical deliverable dose for protein samples at these beamlines. In addition, the cyt *c* samples were exposed using the same syringe pump flow set-up consisting of 100 µm ID microfluidic sample cells. Bottom-up mass spectrometry analysis on irradiated cyt *c* from various sample repeats showed identical and reproducible radiolytic labeling, which is consistent with previous studies (Gupta *et al.*, 2012). Here we report only the dose-response plot of the Met 80 residue (Fig. 5). The irradiated samples from both the beamlines showed similar quantities of modification at all the modified side chains from 250 µs to 2 ms irradiation time, indicating that the delivered dose was comparable between the two beamlines. However, at ALS beamline 5.3.1 the dose can be increased six-fold and the irradiation timescale can further be scaled down to double-digit microsecond irradiation time by using a micro-focused beam of the size used for the Alexa assay (section 3), resulting in improved data quality by reduction of secondary radiation damage. This is especially relevant for studies of complex biological assemblies and membrane proteins. In comparison, the dose obtained using the unfocused beam of size 10 mm (V) × 100 mm (H) at beamline 3.2.1 is ten-fold less, which is sufficient to carry out structural studies on biological important simple globular protein systems such as studies of oligomerization of amyloid proteins, and structural studies on insulin and small antibody–antigen conjugates (Deperalta *et al.*, 2013; Kiselar *et al.*, 2011; Jones *et al.*, 2011; Maleknia *et al.*, 2006).

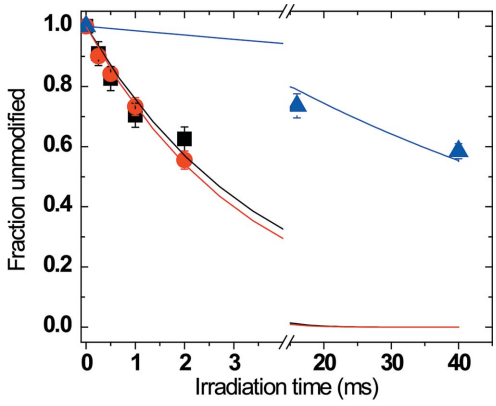

Figure 5
Dose response of residue M80 of cyt *c*. 10 µ*M* of cyt *c* sample in 10 m*M* phosphate buffer, pH 7.0, was irradiated using the flow set-up at beamlines ALS 5.3.1, NSLS X28C and ALS 3.2.1. The deliverable dose on the sample was adjusted to be the same at 5.3.1 and X28C as determined by the standard Alexa assay. The fraction of unmodified peptide at a given exposure was calculated as the unmodified peak area divided by the sum of the unmodified and modified peak areas. The peak areas were calculated from the extracted ion chromatogram, and the site of modification was identified by MS/MS. The solid lines represent single exponential fits with rate constants k = 360 s^{-1}, 330 s^{-1} and 14 s^{-1} for radiolysis carried out at 5.3.1 (black), X28C (red) and 3.2.1 (blue), respectively, with individual points representing the mean of three independent measurements with standard error.

3.4. Sub-millisecond irradiation of a chaperonin assembly at ALS beamline 5.3.1

Chaperonins are large protein complexes consisting of two stacked multi-subunit rings, which open and close in an ATP-dependent manner to create a protected environment for protein folding. In the group II chaperonins from mmcpn, each multi-subunit ring consists of eight 58.5 kDa protein subunits. The full complex possesses 16 such individual subunits and requires a millimolar concentration of ATP to cycle between open and closed states. Thus, mmcpn contains both strong intrinsic and extrinsic hydroxyl radical scavengers and is ideal to test the extent of labeling efficiency using the ALS 5.3.1 focused bending-magnet X-ray source. The beam parameters were set such that deliverable dose was equivalent to that of the previous section. Dose measurements with Alexa 488 showed relatively fast degradation of the fluorophore in mmcpm footprinting buffer, which contains a millimolar concentration of ATP and ∼5% glycerol in a 10 m*M* phosphate buffer (Fig. S4). The absence of any lag phase indicated that the focused high-flux-density X-ray beam provided sufficient dose to compensate for the effect of high concentration of radical scavengers (Gupta *et al.*, 2007*a*). Fig. 6(*a*) shows a representative view of characterization and quantification of •OH-induced modification on the peptide 496–511 on the protein assembly and a linear dose-response plot within 500 µs irradiation time. The predominant modification at Met 508 was confirmed by MS/MS assignment (Fig. 6*b*). We have observed a linear increase up to >10% net modification in several other Met residues with solvent-accessible surface area 10–20 $Å^2$ after subtracting the fixed background modification of 1 to 4% in 'zero' ms samples (Fig. 6*c*). Therefore, our results indicate that an adequate amount of hydroxyl radical dose is deliverable on the sub-millisecond timescale in a megaDalton protein assembly in the presence of significantly high levels of hydroxyl radical scavengers. The use of a micro-focus beam and high-speed microfluidic sample delivery system can further decrease the irradiation time and therefore be used to develop microsecond radiolytic labeling to study protein conformations, an advancement that will widen the scope of the XF experiment to the study of more complex systems in various biological buffer solutions.

3.5. Increase of radiolytic labeling efficiently by use of N_2O saturation of samples

Radiolysis of water by synchrotron X-rays generates solvated electrons and it is well known that N_2O scavenges these electrons to produce one additional •OH per electron (Takahashi *et al.*, 2004) [equation (6)],

$$e^-_{aq} + N_2O + H_2O = {}^{\bullet}OH + N_2 + OH^-. \qquad (6)$$

N_2O also helps to reduce the concentration of solvated electrons, which scavenge the O_2 required in the residue oxidation events [equation (5) and Fig. S3]. Previous electron pulse radiolysis studies on protein samples qualitatively showed that sample solutions saturated with a 4:1 *v*/*v* N_2O:O_2 gas mixture

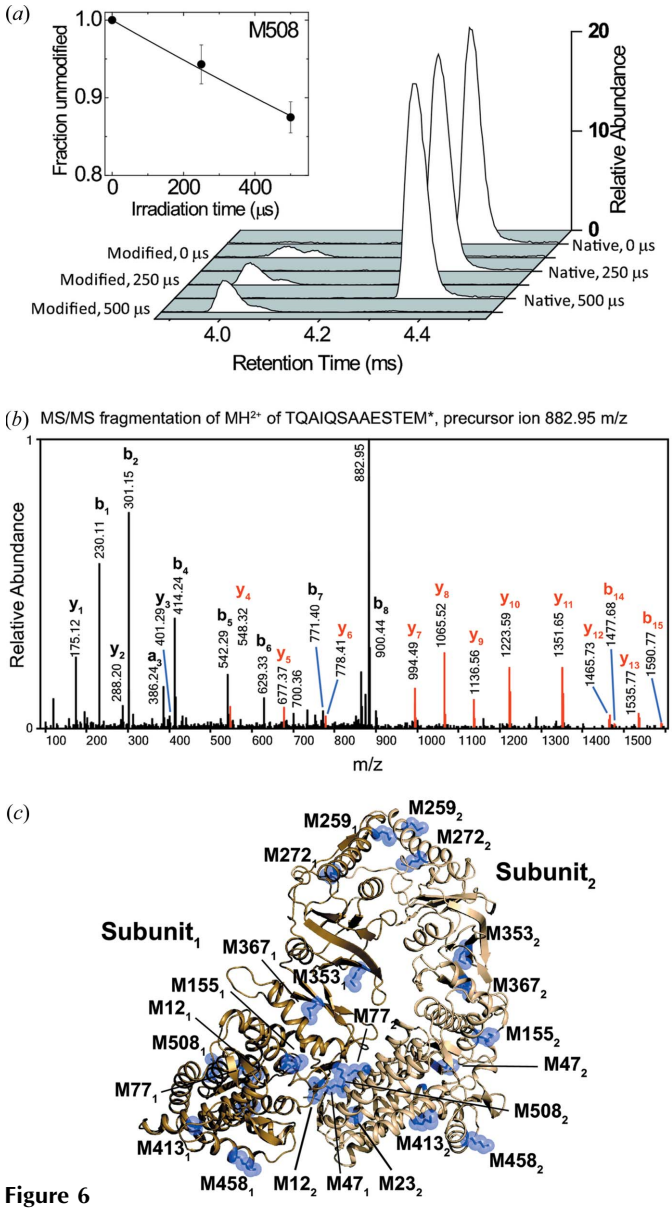

Figure 6
Sub-millisecond irradiation of a megaDalton protein assembly. (*a*) Extracted ion chromatogram showing the increase of the doubly protonated +16 Da modified product of peptide 496–511, TQAIQSAAESTEMLLR (eluted at 4.0 min, 882.95 *m*/*z*) with the increase in irradiation time on the sample solution containing 10 μ*M* mmcpn in 10 m*M* phosphate buffer, pH 7, containing 1 m*M* ATP, 1 m*M* TCEP, ∼5% glycerol and 150 m*M* NaCl. For easy visualization, the abundances of doubly protonated native peaks (eluted at 4.3 min, 874.95 *m*/*z*) are made equal for all the irradiation time points and the corresponding modified peak abundances are adjusted accordingly by multiplication factors. The peak areas are calculated from the extracted ion chromatograms of raw data. The fraction of unmodified peptide at a given exposure is calculated as the unmodified peak area divided by the sum of unmodified and modified peak areas. The ∼3.5% background modification for peptide 496–511 is normalized in the dose-response plot (inset). The solid line represents a single exponential fit with rate constants k = 253.7 s^{-1}, with individual points representing the mean of three independent measurement with standard error. (*b*) The sites of modification are identified by the MS/MS of the double protonated modified precursor ion of 882.95 *m*/*z*. The signature +16 *m*/*z* shift on *y* and *b* fragment ions shown in red indicate modification at M508. (*c*) Pictorial representation of modified Met residues on two adjacent subunits out of the 16 stacked subunits in the protein assembly (3kfb) (Pereira *et al.*, 2010).

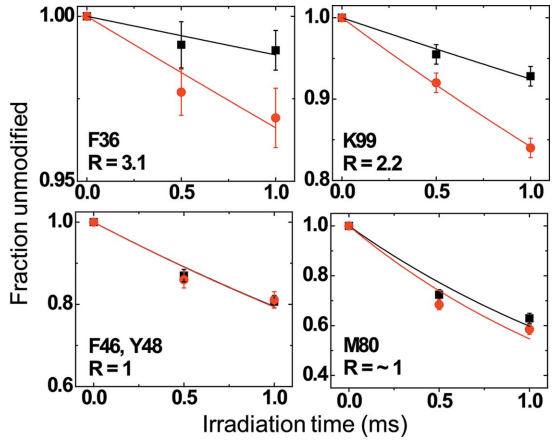

Figure 7
Effect of N_2O saturation on the dose response in cyt *c*. Comparative site-specific dose response plots between N_2O–O_2 (4:1 *v*/*v*) saturated (red) and aerated (black) samples of 10 μ*M* cyt *c* in 10 m*M* phosphate buffer, pH 7.0, irradiated at beamline 5.3.1. Solid lines represent single exponential fits to provide rate constants (k; s^{-1}), which are used to calculate the ratio R = (k, N_2O)/(k, air). The individual points represent the mean of three independent measurements with standard error.

resulted in an increased level of modification observed by mass spectrometry analysis of intact irradiated protein (Watson *et al.*, 2009). However, site-specific changes in the •OH reactivity in the presence of N_2O was not estimated. In our study, the quantitative bottom-up approach of mass spectrometry analysis of the synchrotron X-ray irradiated cyt *c* using beamline 5.3.1 showed a two- to three-fold increase in the modification rate for the side-chain residues F36 and K99, which interact with the bulk water (Fig. 7, top) (Gupta *et al.*, 2012). However, there was no significant increase in the level of modification for peptides with reactive residues F46, Y48 and M80 which are close to the bound water inside the protein cavity (Fig. 7, bottom) (Gupta *et al.*, 2012). These results demonstrate that N_2O saturation of samples can increase the level of modification within a given irradiation interval, reducing the requirement for longer exposure times for the less reactive side chains and increasing data quality for solvent-exposed residues. In addition, it is possible that this technique can be used to distinguish between residues which interact with bound water and residues with surface interactions with the bulk water. We are continuing to implement an N_2O saturation step in the XF experiment in order to both improve data quality and to investigate the possibility of using N_2O to gain additional structural information.

4. Conclusion and future directions

We have successfully demonstrated and extended the XF technique at the ALS using a focused high-flux-density beam from the bending-magnet source at 5.3.1. Beamline conditions required for the microsecond irradiation times were characterized with Alexa, the small globular protein cyt *c*, and a megaDalton chaperonin complex using a newly developed micro-capillary high-flow-rate sample-delivery system. The new flow cell has improved sample irradiation conditions:

sample depth, temperature control, precise flow, low back pressure and low X-ray absorbance. We have shown that N_2O saturation increases data quality by about a three-fold increase in the dose and can provide a larger amplitude of change in the fraction of modification. In collaboration with the Experimental Systems group at the ALS, beamline 5.3.1 will be available for XF users on an as-needed basis. Beamline 5.3.1 will be used for more challenging systems, such as *in vivo* cell studies, large complexes, membrane proteins and microsecond time-resolved studies. In parallel, permission has been granted by the ALS to re-open the previously de-commissioned beamline 3.3.1, and dedicate this beamline to an XF program. Beamline 3.3.1 is located on a white-light bending-magnet source with an acceptance of 6.2×2 mrad, and funds are actively being pursued to purchase a Pt-coated toroidal focusing mirror to be installed outside the shield wall, centered at 11.1 m (two-thirds of the distance) from the source. We anticipate that the focusable beam along with the use of microfluidic sample flow at 3.3.1 will increase the usable flux density at the sample by six- to >30-fold compared with the current bending-magnet NSLS beamline X28C. As the timescale of the XF experiment is pushed even lower, the time resolution will not be limited by the exposure time but by the mixing dead-time. Therefore, future plans include design of a micro-fabricated T-mixer to permit tens of microseconds to single-digit millisecond time-resolved XF, allowing the direct measurement of the dynamics of bound waters, particularly on timescales relevant to catalysis and macromolecular assembly. This technique promises to provide novel insights into the dynamics of bound water in the activation of receptors, the movement of water across pores and channels associated with gating, as well as ligand-dependent structural assembly of macromolecules. The establishment of an XF beamline facility at the ALS not only allows continuation of the X-ray footprinting technique by supporting the NSLS XF users while the NSLS II footprinting beamline is commissioned, but also extends the XF method to the microsecond time regime, and continues development of the XF method for studying the dynamics and structure of ever more challenging biological systems.

The authors would like to thank Jun Hamamoto for assistance on beamline 3.2.1, Kurt Krueger for technical advice and fabrication of the microfluidic capillary cell, Simon Morton for advice and design of a focusing mirror for build-out of beamline 3.3.1, and Rhijuta D'Mello for assisting in beamline experiments at X28C at the NSLS. Funding for this research was provided by an LBNL Laboratory Directed Research and Development (LDRD) grant awarded to CR. The Advanced Light Source is supported by the Director, Office of Science, Office of Basic Energy Sciences, of the US Department of Energy under contract No. DE-AC02-05CH11231. Use of the National Synchrotron Light Source, Brookhaven National Laboratory, was supported by the US Department of Energy, Office of Science, Office of Basic Energy Sciences, under contract No. DE-AC02-98CH10886. The Center for Synchrotron Biosciences at the National Synchrotron Light Sources is supported by NIBIB under P30-EB0966.

References

Adilakshmi, T., Bellur, D. L. & Woodson, S. A. (2008). *Nature (London)*, **455**, 1268–1272.
Adilakshmi, T., Lease, R. A. & Woodson, S. A. (2006). *Nucleic Acids Res.* **34**, e64.
Adilakshmi, T., Soper, S. F. & Woodson, S. A. (2009). *Methods Enzymol.* **468**, 239–258.
Angel, T. E., Gupta, S., Jastrzebska, B., Palczewski, K. & Chance, M. R. (2009). *Proc. Natl Acad. Sci. USA*, **106**, 14367–14372.
Aye, T. T., Low, T. Y. & Sze, S. K. (2005). *Anal. Chem.* **77**, 5814–5822.
Bohon, J., D'Mello, R., Ralston, C., Gupta, S. & Chance, M. R. (2014). *J. Synchrotron Rad.* **21**, 24–31.
Bohon, J., Jennings, L. D., Phillips, C. M., Licht, S. & Chance, M. R. (2008). *Structure*, **16**, 1157–1165.
Buxton, G. V., Greenstock, C. L., Helman, W. P. & Ross, A. B. (1988). *J. Phys. Chem. Ref. Data*, **17**, 374.
Chaudhuri, B. N., Gupta, S., Urban, V. S., Chance, M. R., D'Mello, R., Smith, L., Lyons, K. & Gee, J. (2011). *Biochemistry*, **50**, 1799–1807.
Clatterbuck Soper, S. F., Dator, R. P., Limbach, P. A. & Woodson, S. A. (2013). *Mol. Cell*, **52**, 506–516.
Deperalta, G., Alvarez, M., Bechtel, C., Dong, K., McDonald, R. & Ling, V. (2013). *mAbs* **5**, 86–101.
Dhavan, G. M., Crothers, D. M., Chance, M. R. & Brenowitz, M. (2002). *J. Mol. Biol.* **315**, 1027–1037.
Downard, K. M., Maleknia, S. D. & Akashi, S. (2012). *Rapid Commun. Mass Spectrom.* **26**, 226–230.
Gerega, S. K. & Downard, K. M. (2006). *Bioinformatics*, **22**, 1702–1709.
Guan, J. Q., Takamoto, K., Almo, S. C., Reisler, E. & Chance, M. R. (2005). *Biochemistry*, **44**, 3166–3175.
Gupta, S., Bavro, V. N., D'Mello, R., Tucker, S. J., Vénien-Bryan, C. & Chance, M. R. (2010). *Structure*, **18**, 839–846.
Gupta, S., Chai, J., Cheng, J., D'Mello, R., Chance, M. R. & Fu, D. (2014). *Nature (London)*. In the press.
Gupta, S., Cheng, H., Mollah, A. K., Jamison, E., Morris, S., Chance, M. R., Khrapunov, S. & Brenowitz, M. (2007*b*). *Biochemistry*, **46**, 9886–9898.
Gupta, S., D'Mello, R. & Chance, M. R. (2012). *Proc. Natl Acad. Sci. USA*, **109**, 14882–14887.
Gupta, S., Mangel, W. F., McGrath, W. J., Perek, J. L., Lee, D. W., Takamoto, K. & Chance, M. R. (2004). *Mol. Cell. Proteom.* **3**, 950–959.
Gupta, S., Sullivan, M., Toomey, J., Kiselar, J. & Chance, M. R. (2007*a*). *J. Synchrotron Rad.* **14**, 233–243.
Hambly, D. M. & Gross, M. L. (2005). *J. Am. Soc. Mass Spectrom.* **16**, 2057–2063.
Janik, I., Bartels, D. M. & Jonah, C. D. (2007). *J. Phys. Chem. A*, **111**, 1835–1843.
Jones, L. M., Sperry, J. B., Carroll, J. A. & Gross, M. L. (2011). *Anal. Chem.* **83**, 7657–7661.
Kamal, J. K., Benchaar, S. A., Takamoto, K., Reisler, E. & Chance, M. R. (2007). *Proc. Natl Acad. Sci. USA*, **104**, 7910–7915.
Kamal, J. K. & Chance, M. R. (2008). *Protein Sci.* **17**, 79–94.
Kiselar, J. G. & Chance, M. R. (2010). *J. Mass Spectrom.* **45**, 1373–1382.
Kiselar, J. G., Datt, M., Chance, M. R. & Weiss, M. A. (2011). *J. Biol. Chem.* **286**, 43710–43716.
Kiselar, J. G., Janmey, P. A., Almo, S. C. & Chance, M. R. (2003*a*). *Mol. Cell. Proteom.* **2**, 1120–1132.
Kiselar, J. G., Janmey, P. A., Almo, S. C. & Chance, M. R. (2003*b*). *Proc. Natl Acad. Sci. USA*, **100**, 3942–3947.
Kiselar, J. G., Mahaffy, R., Pollard, T. D., Almo, S. C. & Chance, M. R. (2007). *Proc. Natl Acad. Sci. USA*, **104**, 1552–1557.

Konermann, L., Ahadi, E., Rodriguez, A. D. & Vahidi, S. (2013). *Anal. Chem.* **85**, 2–9.
Kuhn, L. A., Siani, M. A., Pique, M. E., Fisher, C. L., Getzoff, E. D. & Tainer, J. A. (1992). *J. Mol. Biol.* **228**, 13–22.
Kuntz, I. D. Jr, Brassfield, T. S., Law, G. D. & Purcell, G. V. (1969). *Science*, **163**, 1329–1331.
Laganowsky, A., Reading, E., Hopper, J. T. & Robinson, C. V. (2013). *Nat. Protocols*, **8**, 639–651.
Liljenzin, J. (2002). *Radiochemistry and Nuclear Chemistry*, 3rd ed. Oxford: Butterworth-Heinemann.
Ling, J., Cho, C., Guo, L. T., Aerni, H. R., Rinehart, J. & Söll, D. (2012). *Mol. Cell*, **48**, 713–722.
Maleknia, S. D., Chance, M. R. & Downard, K. M. (1999). *Rapid Commun. Mass Spectrom.* **13**, 2352–2358.
Maleknia, S. D. & Downard, K. (2001). *Mass Spectrom. Rev.* **20**, 388–401.
Maleknia, S. D. & Downard, K. M. (2012). *Rapid Commun. Mass Spectrom.* **26**, 2311–2318.
Maleknia, S. D., Reixach, N. & Buxbaum, J. N. (2006). *FEBS J.* **273**, 5400–5406.
Orban, T., Jastrzebska, B., Gupta, S., Wang, B., Miyagi, M., Chance, M. R. & Palczewski, K. (2012). *Structure*, **20**, 826–840.
Oztug Durer, Z. A., Kamal, J. K., Benchaar, S., Chance, M. R. & Reisler, E. (2011). *J. Mol. Biol.* **414**, 204–216.
Padayatti, P. S., Wang, L., Gupta, S., Orban, T., Sun, W., Salom, D., Jordan, S. R., Palczewski, K. & Chance, M. R. (2013). *Mol. Cell. Proteom.* **12**, 1259–1271.
Pearson, R. G. & Williams, E. L. (1987). *J. Polym. Sci. A*, **25**, 565–573.
Pereira, J. H., Ralston, C. Y., Douglas, N. R., Meyer, D., Knee, K. M., Goulet, D. R., King, J. A., Frydman, J. & Adams, P. D. (2010). *J. Biol. Chem.* **285**, 27958–27966.
Pryor, W. A. (1986). *Annu. Rev. Physiol.* **48**, 657–667.
Ralston, C. Y., Sclavi, B., Sullivan, M., Deras, M. L., Woodson, S. A., Chance, M. R. & Brenowitz, M. (2000). *Methods Enzymol.* **317**, 353–368.
Sclavi, B., Sullivan, M., Chance, M. R., Brenowitz, M. & Woodson, S. A. (1998*a*). *Science*, **279**, 1940–1943.
Sclavi, B., Woodson, S., Sullivan, M., Chance, M. & Brenowitz, M. (1998*b*). *Methods Enzymol.* **295**, 379–402.
Shacter, E. (2000). *Drug Metab. Rev.* **32**, 307–326.
Sullivan, M. R., Rekhi, S., Bohon, J., Gupta, S., Abel, D., Toomey, J. & Chance, M. R. (2008). *Rev. Sci. Instrum.* **79**, 025101.
Takahashi, K., Ohgami, S., Koyama, Y., Sawamura, S., Marin, T. W., Bartels, D. M. & Jonah, C. D. (2004). *Chem. Phys. Lett.* **383**, 445–450.
Watson, C., Janik, I., Zhuang, T., Charvátová, O., Woods, R. J. & Sharp, J. S. (2009). *Anal. Chem.* **81**, 2496–2505.
Wong, J. W., Maleknia, S. D. & Downard, K. M. (2005). *J. Am. Soc. Mass Spectrom.* **16**, 225–233.
Xu, G. & Chance, M. R. (2007). *Chem. Rev.* **107**, 3514–3543.
Yuan, S., Goldberg, K. A., Yashchuk, V. V., Celectre, R., Warwick, T. & McKinney, W. R. (2011). *Nucl. Instrum. Methods Phys. Res. A*, **635**, S58–S63.